Article

In Situ Droplet Microgoniometry Using Optical Microscopy

Hyeongyun Cha, Jingcheng Ma, Young Seong Kim,
Longnan Li, Luwen Sun, Jiashuo Tong, and Nenad Miljkovic

ACS Nano, **Just Accepted Manuscript** • DOI: 10.1021/acsnano.9b06687 • Publication Date (Web): 09 Oct 2019

In Situ Droplet Microgoniometry Using Optical Microscopy

Hyeongyun Cha[1,4], Jingcheng Ma[1], Young Seong Kim[1], Longnan Li[1], Luwen Sun[1], Jiashuo Tong[1], and Nenad Miljkovic[1,2,3,4,*]

[1]*Department of Mechanical Science and Engineering, University of Illinois at Urbana-Champaign, Urbana, Illinois 61801, USA*

[2]*Department of Electrical and Computer Engineering, University of Illinois at Urbana-Champaign, Urbana, Illinois 61801, USA*

[3]*Materials Research Laboratory, University of Illinois at Urbana-Champaign, Urbana, Illinois 61801, USA*

[4]*International Institute for Carbon Neutral Energy Research (WPI-I2CNER), Kyushu University, 744 Moto-oka, Nishi-ku, Fukuoka 819-0395, Japan*

*Corresponding Author E-mail: nmiljkov@illinois.edu

ABSTRACT

Solid-liquid interactions are ubiquitous phenomena in the nature and industry. Wettability of a liquid on a solid is governed by the chemical heterogeneity and physical roughness of the solid surface and can be characterized by measuring the advancing and receding contact angles of the liquid droplet residing on the solid. To characterize contact angle, goniometry or the Wilhelmy plate method have been widely used. Although powerful, these methods have difficulty characterizing microdroplets, can be cumbersome and expensive, and have trouble handling surfaces with local wetting heterogeneity and deformed non-circular contact lines. Furthermore, past methods are incapable of measuring contact angle *in situ* during experiments (*e.g.* condensation). Here, we develop simple yet powerful contact angle measurement techniques using conventional optical microscopy that utilizes focal plane shift imaging, ray optics, and wave interference. We used our techniques to study the wetting characteristics for a wide range of water droplet diameters (3 μm < D < 600 μm) and apparent contact angles ($0° \leq \theta^{\mathrm{app}} \leq 180°$). The outcomes of this work establish a powerful tool to more easily and rapidly characterize microscale droplet advancing and receding contact angles.

KEYWORDS: hydrophilic, hydrophobic, superhydrophobic, contact angle, focal plane shift imaging, ray optics, interference

Solid-liquid interactions govern a plethora of natural and engineering processes such as cleaning,[1] printing,[2] lubrication,[3] microfluidics,[4] photolithography,[5] and heat transfer.[6] The degree of wetting can be determined by the equilibrium contact angle which was first rigorously introduced by Thomas Young in 1805 by balancing the forces at the three phase contact line on a homogeneous and smooth surface.[7, 8] In practical engineering applications, surface roughness,[9] chemical heterogeneity,[10] and deformation[11] result in the formation of contact angle hysteresis ($\Delta\theta$) defined as the difference between the apparent advancing (θ_a) and apparent receding (θ_r) contact angles ($\Delta\theta = \theta_a - \theta_r$).[12] Since the contact angle hysteresis governs the mobility of droplets on a surface,[13] a number of studies have attempted to achieve low contact angle hysteresis to improve droplet mobility. With recent advent of chemical coatings and micro/nanofabrication, non-wetting hydrophobic and superhydrophobic surfaces have received much attention due to their potential to enhance a variety of water-based applications such as self-cleaning,[14] anti-icing,[15] and heat transfer.[16] Therefore, accurate knowledge of the liquid droplet or vapor bubble advancing and receding contact angles and their corresponding contact angle hysteresis is crucial.

Past experimental methods to characterize the apparent contact angle have utilized mainly side-view imaging techniques such as the Wilhelmy plate[17, 18] and the sessile droplet[19] methods. Although powerful, the Wilhelmy plate method is relatively complicated and cannot work with droplets. The sessile droplet method is the most common technique used today mainly due to its low cost (see Table S1), simplicity, and reasonable accuracy.[20-22] However, state of the art goniometric methods have difficulties characterizing droplet with length scales smaller than ~1 mm due to the difficulty in dispensing small droplets using syringes. Although piezoelectric microgoniometry has enabled the study of microdroplets,[23, 24] its inability to handle certain low surface tension fluids, along with its high cost (see Table S1), makes its utilization limited. More

importantly, the past techniques image from the side, making it difficult to resolve contact line shape, and to conduct measurements *in situ* (*i.e.* simultaneous for many droplets). Recently, laser scanning confocal microscopy has enabled the accurate measurement of contact angles,[25, 26] however, it is inherently slow and expensive (see Table S1), limiting implantation in smaller laboratory settings.[27] To characterize the contact line and measure the contact angle simultaneously, a considerable amount of work has focused on developing top-view optical techniques using reflection, refraction, or interference. Although accurate, these techniques are not only complex to implement due to the need for specialized optics,[28-31] they are limited to the measurement of droplet having low intrinsic contact angles ($\theta < 30°$).[31-33]

Here, we develop a number of rather simple yet highly powerful single-camera optical microscopy techniques capable of measuring the apparent advancing and apparent receding contact angles for a wide range of droplet sizes ($10 \leq D \leq 600$ μm, where D is the droplet diameter) and surface wettability ($0° \leq \theta^{\mathrm{app}} \leq 180°$, where θ^{app} is the apparent contact angle on the surface). First, we utilized focal plane manipulation (FPSI, focal plane shift imaging)[34, 35] to enable the measurement of droplets characterized by high contact angles ($\theta^{\mathrm{app}} > 90°$). Furthermore, we develop an alternative contact angle measurement technique through the use of ray optics simulations. For hydrophilic surfaces ($\theta^{\mathrm{app}} < 90°$), we developed a modified interferometry technique utilizing interferometric fringe formation. To benchmark our techniques, we compare our results with conventional microgoniometric techniques in addition to conducting a rigorous error analysis to establish the limits of our approaches. The outcomes of this work establish a powerful imaging platform as a tool to enable rapid, *in situ*, characterization of microscale droplet advancing and receding contact angles for a variety of working fluids.

RESULTS AND DISCUSSION

Experiment. Smooth silicon (Si) wafers (P/B <100> 0-100 Ω-cm, University Wafer) and nanostructured boehmite (AlO(OH)) surfaces were used as model substrates for hydrophilic, hydrophobic, and superhydrophobic surfaces (Fig. 1). To create nanostructured boehmite surfaces, aluminum (Al) tabs were immersed into hot water (≈90 °C) for 10 min.[36, 37] Nanostructured boehmite surfaces with sharp knife-like structures were formed having length scales approaching ≈ 90 nm. To prepare the hydrophilic surface, Polymethyl methacrylate (PMMA, CAS no. 100-66-3, MicroChem) was spun-coated on the smooth Si wafer for 45 seconds at 2,000 RPM, followed by pre-baking on a hot plate at 180°C for 50 seconds (Fig. 1a). To create hydrophobic and superhydrophobic surfaces, heptadecafluorodecyltrimethoxy-silane (HTMS, CAS no. 83048-65-1, Sigma-Aldrich) was deposited on both the smooth Si wafer (Fig. 1b) and nanostructured boehmite surfaces (Fig 1c, Fig. S1a) using vapor phase deposition.[38, 39] Microgoniometric measurements (MCA-3, Kyowa Interface Science) of ≈50 nL droplets on the hydrophilic Si, hydrophobic Si, and superhydrophobic boehmite surfaces showed apparent advancing/receding contact angles of θ_a = 114.9 ± 1.3°/θ_r = 107.4 ± 1.4°, θ_a = 164.9 ± 3°/θ_r = 162.9 ± 4°, and θ_a = 69 ± 1° and θ_r = 40 ± 1°, respectively. A detailed description of the sample fabrication and functionalization steps is shown in the Methods.

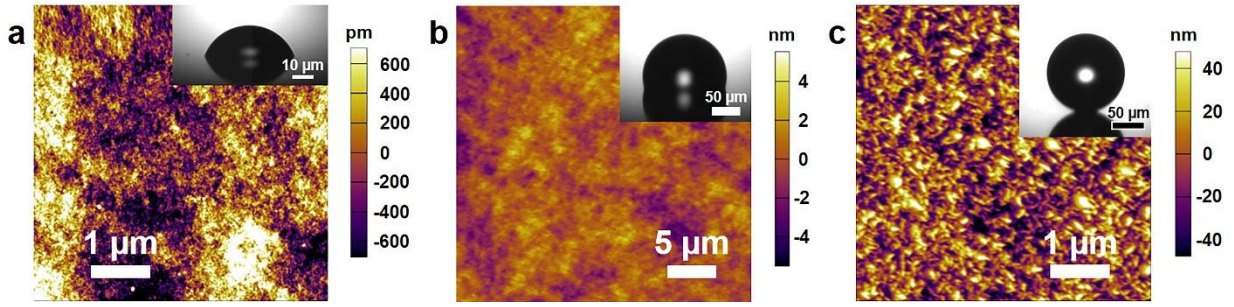

Figure 1. Atomic force microscopy images of a (a) PMMA-coated smooth Si wafer, (b) HTMS-coated smooth Si wafer, and (c) HTMS-coated nanostructured boehmite surface. Inset images: microscopic water droplets residing in the apparent advancing state. The surfaces in (a−c) had advancing/receding contact angles of θ_a = 69 ± 1°/θ_r = 40 ± 1°, and 114.9 ± 1.3°/107.4 ± 1.4°, and 165.3 ± 3.0°/160.1 ± 4.5°, respectively.

Focal Plane Shift Imaging. To measure the advancing and receding contact angles using conventional microscopy (Fig. 2a), a monochrome camera (DS-Qi2, Nikon) was attached to an upright optical microscope (Eclipse LV100, Nikon). Illumination was supplied by a light emitting diode (LED) light source (SOLA SM II Light Engine, Lumencor). The LED light source was specifically chosen for its high-intensity, low-power consumption (2.5 W) and narrow spectral range (380−680 nm) in order to minimize heat generation at the surface due to light absorption.

Hydrophobic and superhydrophobic surfaces were horizontally placed on a cold stage (TP104SC-mK2000A, Instec) by applying a thin layer of thermal grease (Omegatherm, Omega, thermal conductivity of 2.2 W/(m·K)), followed by reducing temperature to T_w = 1 ± 0.5°C to induce condensation and increasing temperature to T_w = 30 ± 0.5°C to induce the evaporation in a laboratory air environment having temperature T_{air} = 23 ± 0.5°C and a relative humidity ϕ = 45 ± 5% (RO120, Roscid). Throughout our experiments, the Bond number of microscale droplets (R < 300 µm) was much smaller than unity ($Bo = \rho g R^2/\gamma \ll 1$, where ρ is the density of the liquid, g is the gravitational acceleration, R is the radius of curvature, and γ is the surface tension) ensuring that droplet shapes formed spherical caps.

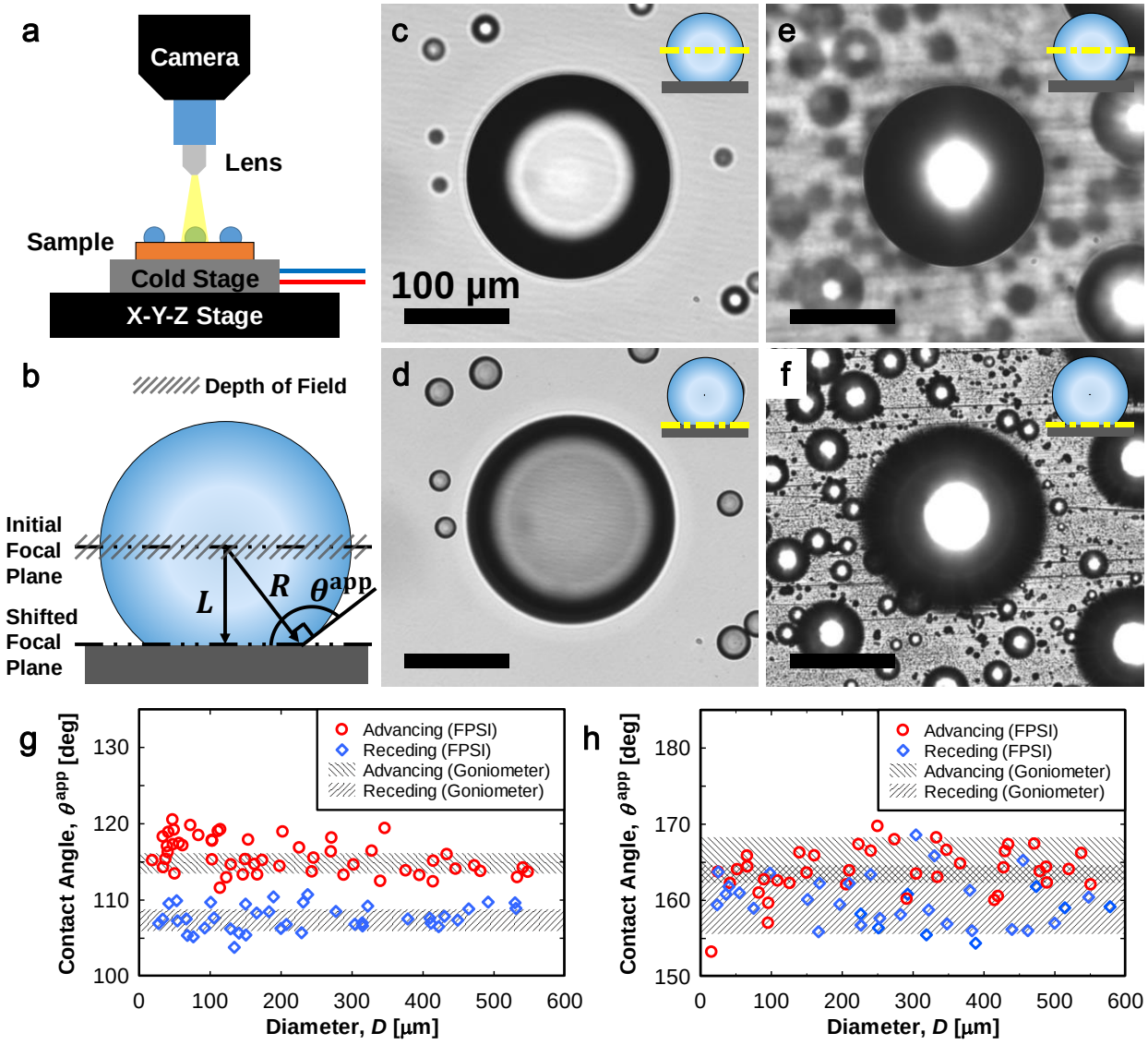

Figure 2. Schematics of the (a) top-view experimental setup and (b) focal plane shift imaging (FPSI) method for contact angle measurement on the hydrophobic and superhydrophobic surfaces ($\theta^{app} > 90^o$). The FPSI contact angle measurement relies on obtaining droplet radius, R, by placing the focal plane in the middle of the target droplet, and shifting the focal plane on the substrate by a known distance, L. Top-view optical microscopy images of a condensing water droplet when the focal plane is placed (c) in the middle of the droplet and (d) on the HTMS coated Si wafer, (e) in the middle of the droplet and (f) on the HTMS coated boehmite surface. Insets of (c–f) show schematics of the location of the focal plane (depicted by the yellow dash-dot line). Experimentally measured apparent advancing and apparent receding contact angles as a function of droplet diameter, D, on an HTMS-coated (g) smooth Si wafer (θ_a = 114.9 ± 1.3°/θ_r = 107.4 ± 1.4°) and (h) nanostructured boehmite surface (θ_a = 165 ± 3°/θ_r = 160 ± 5°). Red and blue shaded areas represent the results of microgoniometric measurements, while red and blue symbols represent the results of FPSI measurements.

The FPSI technique (Fig. 2b) relies on two steps: (1) measuring the initial conditions with the focal plane placed in the middle (center) of the droplet (Fig. 2c, e), and (2) shifting the focal plane to the base of the droplet (solid surface) to measure the distance between the middle and bottom of the droplet (Fig. 2d, f). By analyzing the radius of curvature, R, and middle-to-base distance, L, of the sessile droplet, the apparent advancing and receding contact angles can be computed by

$$\theta^{\mathrm{app}} = \frac{\pi}{2} + \sin^{-1}\left(\frac{L}{R}\right) \quad (1)$$

To rigorously verify that the focal plane is placed as close to the middle or bottom of the droplet, the depth of field of the microscope objectives must be small enough to observe the sharp contour of the droplet (Fig. S2). The depth of field for the objectives used in this experiment were 1.36 μm, 0.75 μm, and 0.43 μm for 20X (TU Plan Fluor EPI, Nikon), 50X (TU Plan EPI ELWD, Nikon), and 100X (TU Plan EPI ELWD, Nikon) objectives, respectively, which are much smaller than the droplet length scale in this study. Moreover, nanoscale defects or agglomerates[40] on the smooth hydrophobic surface and micro/nanostructures on the superhydrophobic surface were used to focus on the substrate surface.

We benchmarked the FPSI-based technique by characterizing the advancing and receding contact angles of smooth HTMS-coated Si wafers (Fig. 2g) and comparing the measured values to those obtained using microgoniometry (shaded area in Fig. 2g, h). Differences between the two techniques were within ±5 %, showing that the FPSI contact angle results agree well with classical goniometric measurements (root mean square (RMS) error: $\mathrm{RMS}_{\theta a}$ = 2.9; $\mathrm{RMS}_{\theta r}$ = 1.8 degrees). After demonstrating the validity of FPSI technique on the smooth Si surface, we measured the apparent advancing and apparent receding contact angles on the HTMS-coated nanostructured

boehmite surface (Fig. 2h). For the superhydrophobic surface, the data showed more scatter ($RMS_{\theta a}$ = 3.3; $RMS_{\theta r}$ = 3.4). Due to the spherical geometry of the droplets, small changes in L cause large changes in the corresponding calculated apparent contact angle (Eq. 1).

Interestingly, the FPSI measurement revealed the presence of bright white circles surrounded by dark annuli within the droplet (Fig. 2c−f). The size of the bright circle varied depending on the location of the focal plane as well as the droplet apparent contact angle. The diameter of the bright circle reduced when the focal plane was placed closer to the center of the droplet (Fig. 2c), or when the apparent contact angle of the droplet increased (Fig. 2e−f). To study the physics governing the development of the bright circle, and to test whether they can be used to quantify surface wetting using FPSI, we turned to geometrical (ray) optics simulations.

Ray Optics Method. To simulate the path of light rays through the liquid water droplet, the circular segment of a droplet having an apparent contact angle with a defined refractive index was placed on top of a reflective flat substrate. Both an open source simulation platform[41] and MATLAB (R2018a, MathWorks) were used to conduct two-dimensional (2D) axisymmetric simulations. The simulation domain was 2D, appropriate due to the axisymmetric nature of the droplet. A collimated beam of light rays emanating from the horizontal wall bounding the top of the simulation was applied. This boundary condition emulates the illumination provided from the optical microscope objective during experiments. The LED light source used in the experiments had a narrow spectral range of 380−680 nm, which corresponded to the wavelength-dependent index of refraction of ≈1.33 for liquid water at atmospheric pressure and test temperature range (1 < T_w < 30 °C).[42] The path of the rays through the water droplet for a variety of apparent contact angles (0° < θ^{app} <180°) was simulated (Video S1).

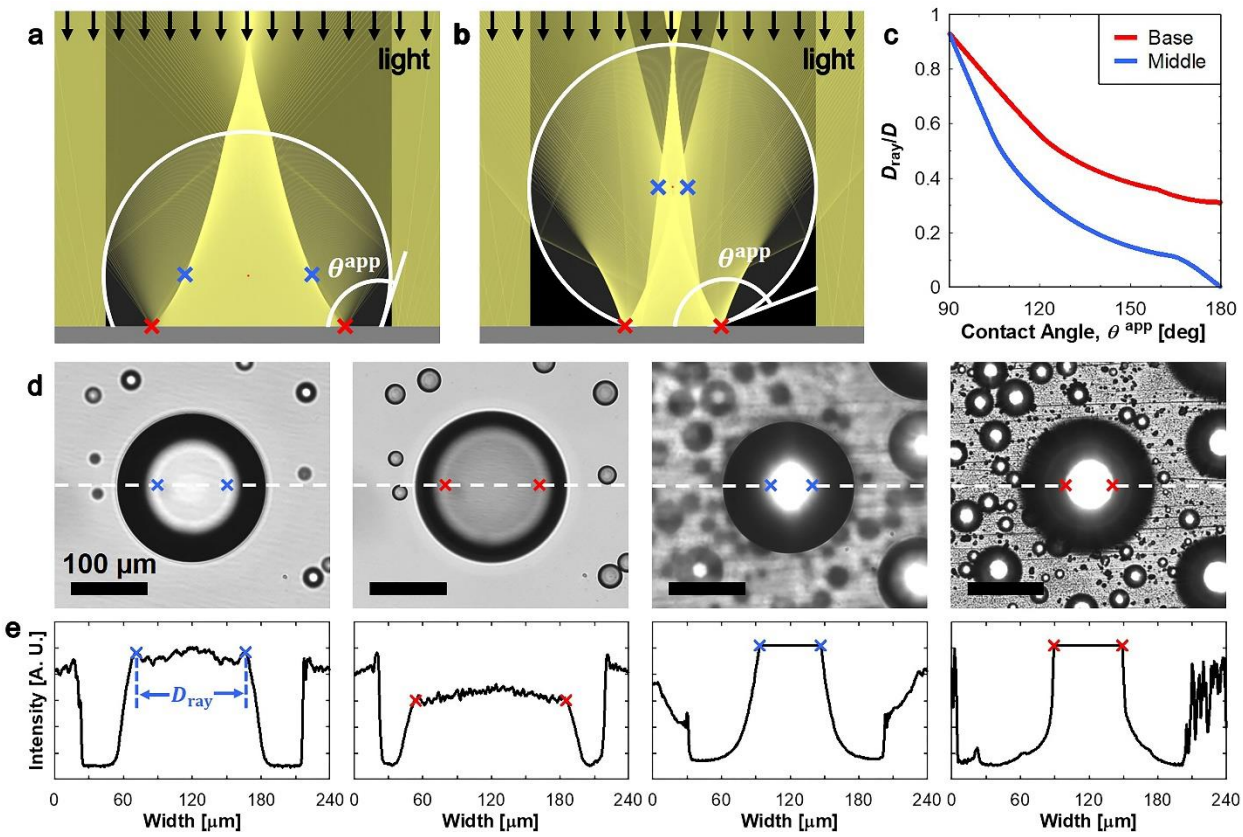

Figure 3. Ray optics simulations of collimated light trajectories through water droplets having apparent advancing contact angles of (a) 110° and (b) 165°, corresponding to the experiments shown in Figure 2. Red and blue cross symbols show the location where the focal plane intersects the bright circle at the bottom and the center of the droplets, respectively. (c) Ratio of the bright circle diameter, D_{ray}, to maximum droplet diameter, D, as a function of apparent contact angle, θ^{app}. See Supporting Information Video S1 for a video of the simulation showing the full range of apparent contact angles, $0° < \theta^{app} < 180°$. (d) Top-view optical microscopy images with (e) corresponding intensity profiles along the white dotted line segments across the droplets shown in (d). Blue and red cross symbols in (e) indicate where the light intensities reach local maxima, the distance between of which represents D_{ray}.

Figures 3a and 3b show the simulated ray paths traveling through the water droplet on the hydrophobic and superhydrophobic surfaces with apparent contact angles of θ^{app} = 110° and 165°, respectively. Once the beam of rays passes through the liquid-air interface, the rays refract with respect to the interface normal. The rays then reflect from the surface, and travel back outside of the droplet towards the top. Since the path of the ray relative to the droplet is always the same, we

can obtain the relationship between the diameter of the droplet, D, and the ray, D_{ray}, for both focal plane locations (droplet base and droplet center) as a function of the surface wettability. Figure 3c shows that D_{ray}/D linearly decreases for the region $90° < \theta^{\mathrm{app}} < 110°$. However, refracted rays begin to intersect for $\theta^{\mathrm{app}} > 110°$, showing a further non-linear decrease in D_{ray}/D. For $\theta^{\mathrm{app}} > 160°$, the rays refract more than once after crossing the liquid-air interface prior to reaching the bottom of the droplet. To experimentally characterize the contact angle using the developed relationship in Fig. 3c, the diameter of the droplet was first measured. Then, the diameter of the bright light circle inside the droplet equator was measured, defined as the distance between two local maxima and quantified by analyzing the light intensity along the line trace across the middle of the droplets (Fig. 3d, e). Interestingly, our ray optics simulations reveal a second method, complimentary to the aforementioned FPSI approach, to experimentally measure the contact angle of droplets without the need to characterize focal plane motion (L).

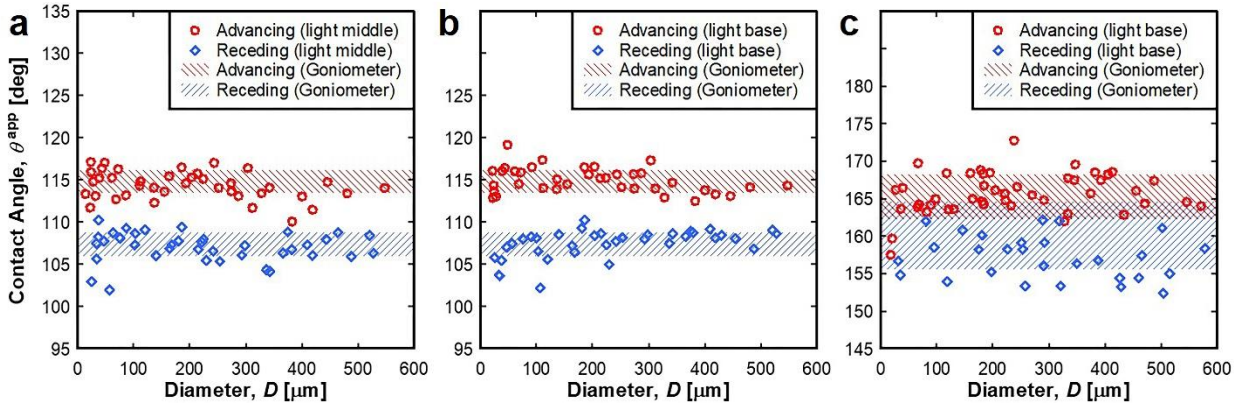

Figure 4. Experimentally measured apparent advancing and apparent receding contact angles, θ^{app}, as a function of droplet diameter, D, for the HTMS coated smooth Si wafer using the ray optics method at the (a) middle and (b) bottom of the droplet. (c) Experimentally measured apparent contact angles as a function of D for HTMS coated nanostructured boehmite using the ray optics method at the bottom of a droplet. Red and blue shaded areas represent the results obtained using independent microgoniometric measurements. Red and blue symbols represent the contact angles measured using the ray optics method.

We benchmarked the single-plane ray optics method by characterizing the advancing and receding contact angles of a smooth HTMS-coated Si wafer (Fig. 4a, b) and compared the measured values to those obtained with microgoniometry. Differences in θ^{app} between the two techniques were shown to be within ±5 % ($\mathrm{RMS}_{\theta \mathrm{a,base}}$ = 1.5; $\mathrm{RMS}_{\theta \mathrm{r,base}}$ = 1.8; $\mathrm{RMS}_{\theta \mathrm{a,middle}}$ = 1.8; $\mathrm{RMS}_{\theta \mathrm{r,middle}}$ = 1.7;). For our superhydrophobic surfaces, the surface consists of sharp knife-like nanostructures having length scales approaching ≈90 nm. When incident light approaches the surface, it undergoes diffuse reflection (Fig. S3). Therefore, the shape of the bright circle inside the droplet was not completely circular and difficult to measure accurately, while the ray beam at the bottom of the droplet was circular regardless of the surface structures. Figure 4c shows the contact angle measurement on a superhydrophobic boehmite surface using the diameter of the bright circle at the bottom of the droplet. The results are comparable with those measured using microgoniometry, but show higher scatter when compared to the smooth HTMS-coated hydrophobic surface ($\mathrm{RMS}_{\theta \mathrm{a}}$ = 2.8; $\mathrm{RMS}_{\theta \mathrm{r}}$ = 4.0). Analogous to the high sensitivity of θ^{app} to small changes in L in the FPSI technique (Eq. 1), the change in D_{ray}/D is steeper as the contact angle increases, resulting in larger uncertainty in contact angle measurement as the droplet becomes more spherical.

Droplets having low apparent contact angles ($\theta^{\mathrm{app}} < 90°$) were not considered in the FPSI and ray optics methods. When the incident ray travels from a medium having higher refractive index, n_1, to a medium having lower refractive index, n_2, the refracted ray will bend toward the boundary. If the angle of incident light is greater than critical angle, $\theta_{\mathrm{c}} = \sin^{-1}(n_2/n_1)$, the incident ray will not cross the interface and will be totally reflected. In our study, the critical angle at the boundary between the liquid water and the air was determined to be θ_{c} = 48.5°. On a hydrophilic surface, as θ^{app} becomes smaller than 90°, the angle of incidence becomes greater

than the critical angle and undergoes total internal reflection (Fig. S4, Video S1). Therefore, the ray optics method does not work on hydrophilic surfaces since the diameter of the bright circle cannot be measured.

Furthermore, when the incident ray travels back outside the droplet, we observed that the width of the concentrated ray (bright circle) was wider than the tip of the droplet from the ray optics simulations (Fig. S4). The simulation result shows that the top of the droplet is not easily distinguishable. Indeed, we were not able to measure L for the FPSI method, indicating that the FPSI methods is also not suitable for hydrophilic surfaces. To enable the characterization of hydrophilic state droplets, we developed a modified optical interferometry method using monochromatic light.

Wave Optics Method. When a monochromatic light wave travels through the droplet liquid−vapor interface, part of the wave will be reflected, with the rest of the wave propagating through the droplet only to be reflected from the bottom substrate. As the transmitted light wave having a longer optical path comes back to the liquid−vapor interface, the coherent waves combine and superpose, resulting in concentric ring patterns of bright and dark fringes. Constructive and destructive interferences are created when coherent waves are in phase or out of phase, respectively. Termed Newton's rings, the interference pattern has been used to determine the profiles of fluid layers,[32, 43] vapor gaps,[44, 45] films,[46, 47] and blisters[48-50]. The droplet apparent contact angle can be calculated after measuring the height of the fluid layer by counting interferometric fringes, $h = j\lambda/2n$, where j is the number of interferometric fringes, λ is the wavelength of light, and n is the fluid index or refraction. Although promising, the fringe counting method is only suitable for $\theta^{\mathrm{app}} < 30°$, where the distance between two fringes is large enough to enable distinct fringe counting.

When $\theta^{app} > 30°$, the height along the droplet periphery varies drastically, making it untenable to resolve fringes.[32, 43] To overcome these difficulties, we developed a simple image analysis technique using optical interference to determine θ^{app} for hydrophilic droplets having $\theta^{app} > 30°$.

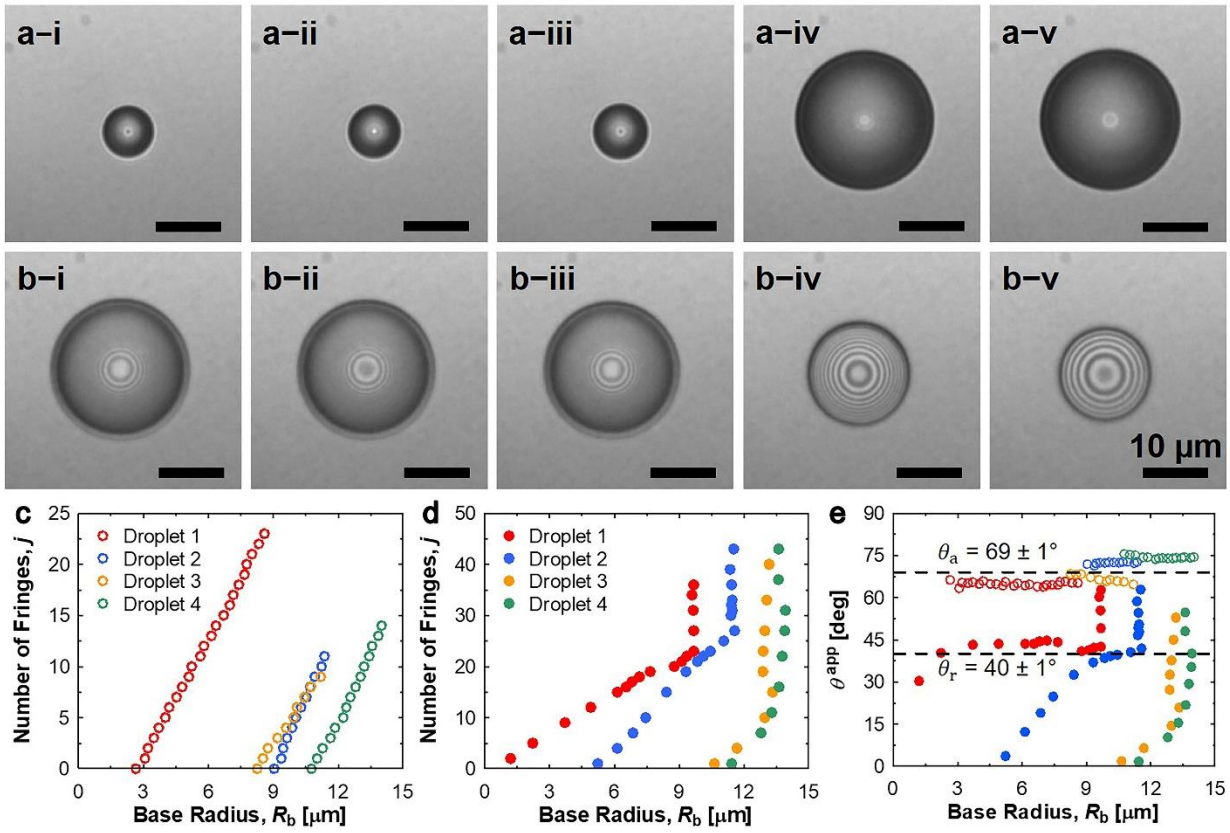

Figure 5. Top-view optical microscopy images of water droplet evolution on a PMMA coated hydrophilic Si wafer surface in the (a) advancing state and (b) receding state. Bright/dark fringes are present near the center of the droplet while fringes at the outer edge are not visible. As the contact angle decreases below $\theta^{app} < 30°$, towards the end of the receding state (b–iv, v), interferometric fringes become visible. The droplet shown is denoted as 'Droplet 2' in (c–e). Number of fringes formed, j, as a function of droplet base radius, R_b, for four different evolving droplets during (c) water vapor condensation and (d) evaporation. (e) Experimentally measured contact angles on the PMMA coated smooth Si wafer (θ_a = 69 ± 1°/θ_r = 40 ± 1°) using the wave optics method (Eq. 4). Dotted horizontal black lines represent the advancing and receding contact angles measured using side-view microgoniometry.

To measure the contact angle on a hydrophilic surface, water droplets were first condensed on the hydrophilic PMMA surface ($\theta_a \approx 69°$, $\theta_r \approx 40°$) and examined under a monochromatic light source using a bandpass excitation filter (λ = 435 ± 10 nm). Videos were recorded with a frame rate of 2 frames per second (FPS) or higher, faster than the fringe shifting rate of ≈1 FPS. Figure 5 shows the evolution of a water droplet during condensation (Fig. 5a) and evaporation (Fig. 5b). Unlike previously studied low contact angle droplets,[32, 43] interferometric fringes tended to merge together and made it difficult to distinguish each other. Although it was not feasible to count the total number of fringes (Video S2), we observed that bright and dark fringes were clearly distinguishable near the center of the droplet during condensation (Fig. 5a) and merged during evaporation (Fig. 5b). Thus, the relative growth of the droplet central height can be calculated by:

$$\Delta h = \frac{\Delta j \lambda}{2n}, \tag{2}$$

while the relative growth of the droplet base radius, ΔR_b, can be measured directly from top-view microscopy. Note that the droplet base radius, R_b, is observed for hydrophilic droplets, while the radius of curvature, R, is observed for hydrophobic droplets. Assuming a truncated spherical cap droplet geometry (Fig. S5), Δh can be related to ΔR_b and the apparent contact angle θ^{app} *via*:

$$\Delta h = \Delta R_b \frac{1 - \cos\theta^{app}}{\sin\theta^{app}}, \tag{3}$$

and the corresponding apparent contact angle can be calculated after re-arranging Eq. (3):

$$\theta^{app} = \cos^{-1}\left(\frac{1 - (\Delta h/\Delta R_b)^2}{1 + (\Delta h/\Delta R_b)^2}\right). \tag{4}$$

Figures 5c and 5d show the number of fringes formed and eliminated as a function of the droplet base radius during water vapor condensation and evaporation, respectively. Figure 5e shows the corresponding contact angle measurements calculated using Eq. (4). The results show

that the contact angle measurement using the developed interference fringe counting method had excellent agreement with microgoniometric contact angle measurements (dotted black horizontal lines). In the advancing state, the droplets grew in the constant contact angle mode. In the receding state, the contact angle first decreased to the receding contact angle from the advancing contact angle with a constant base radius, followed by a constant receding contact angle mode due to shrinking of the base radius. During late stages of the receding phase, droplets began to pin at surface defects,[51-53] resulting in a further reduction of the receding contact angle. As evidenced from the experimental data, droplets 3 and 4 (Fig. 5c–e) were strongly affected by pinning, resulting in receding contact angle collapse to 0° during the final stages of evaporation. Unlike classical microgoniometry, the wave optics method demonstrates the advantage of fringe counting by enabling the analysis of multiple droplets within a single field of view, and hence, enabling the study of spatially heterogeneous wetting and defect (pinning) site identification (*i.e.* droplets 3 and 4 of Fig. 5).

Measurement Uncertainty. The accuracy of the FPSI and wave optics measurement techniques mainly relies on the resolution of the optical microscope in use. The lateral resolution, $d_{\text{lateral}} = 1.22\lambda/(2NA)$, is better than the axial resolution, $d_{\text{axial}} = 2n\lambda/(NA)^2$, by at least a factor of three in a fixed focal plane, where NA represents the numerical aperture of the objective. In general, objective lenses are capable of resolving ≈ 200 nm in the imaging plane, while they can distinguish at most ≈ 700 nm in the axial direction.[54] The accuracy of the FPSI method is limited by both the lateral and axial resolution, the ray optics method is limited by lateral resolution and material properties (refractive index), while classical interferometry is limited by lateral resolution, light wavelength, and material properties.

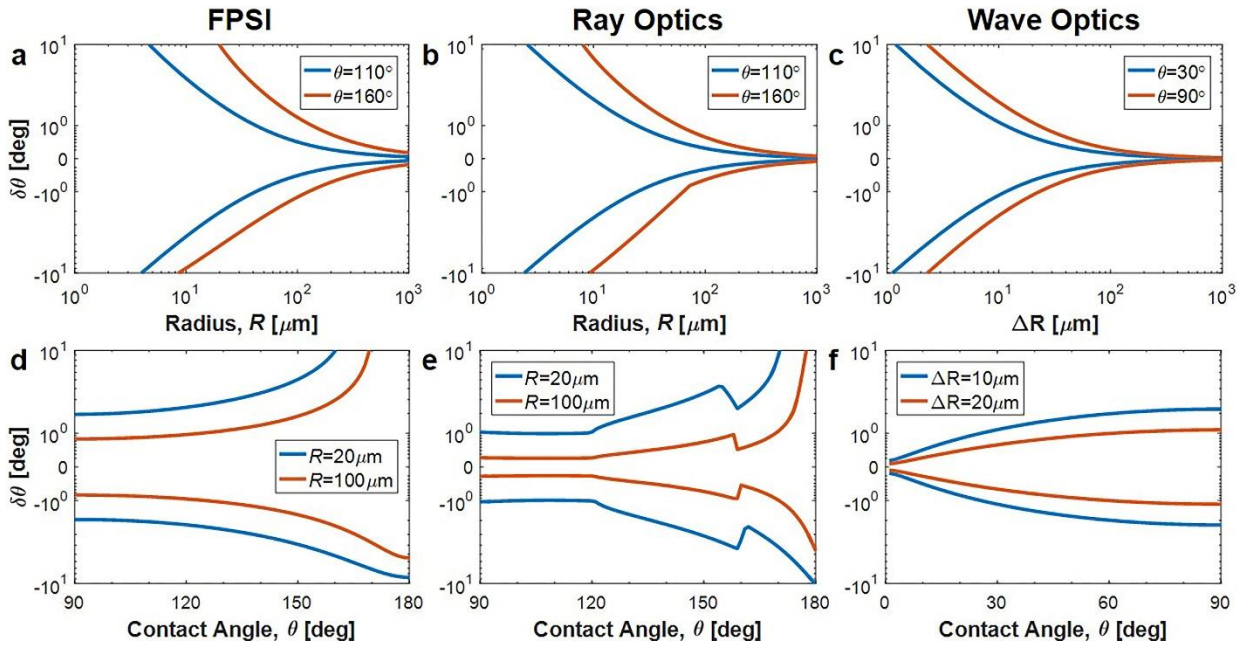

Figure 6. Propagation of uncertainty as a function of (a−c) droplet size and (d−f) contact angle for the FPSI, ray optics method, and wave optics method, respectively. The uncertainty of each technique stems from the lateral and axial resolution of the optical microscope, the wavelength of light, and material properties.

To characterize the accuracy of our developed methods, we utilized error propagation analysis assuming the uncertainties of measured quantities are independent and random:[55]

$$\delta q = \sqrt{\left(\frac{\partial q}{\partial x_1}\delta x_1\right)^2 + \cdots + \left(\frac{\partial q}{\partial x_\mathrm{n}}\delta x_\mathrm{n}\right)^2}, \quad (5)$$

where x_1, …, x_n are measured quantities with corresponding uncertainties δx_1, …, δx_n that are measured to compute the quantity of interest, q having an uncertainty δq. By solving Eq. (5) for all contact angle measurement techniques defined by Eq. (1), Eq. (4), and Fig. 3c, the uncertainties of each method were characterized (Fig. 6). Although FPSI showed the largest uncertainty among the three techniques, the uncertainty of the FPSI method was $\delta\theta < 3°$ even for droplets having radii as small as 20 μm on a hydrophobic surface (Fig. 6a, d). The ray optics method (Fig. 6b, e) showed higher accuracy since it mainly depended on lateral resolution of the microscope. The

wave optics method took advantage of the narrow spectral range of light and showed uncertainty of $0.5° < \delta\theta < 1.5°$ for droplets having radii as small as 20 μm on surfaces with $30° < \theta^{app} < 90°$, respectively (Fig. 6c, f). In general, for all cases, the uncertainties increase as θ^{app} increases due to the larger variation of droplet shape at higher apparent contact angles. We also note that the contact angle may be affected by the line tension as the droplets approach submicron or millimeter lengthscales.[56, 57]

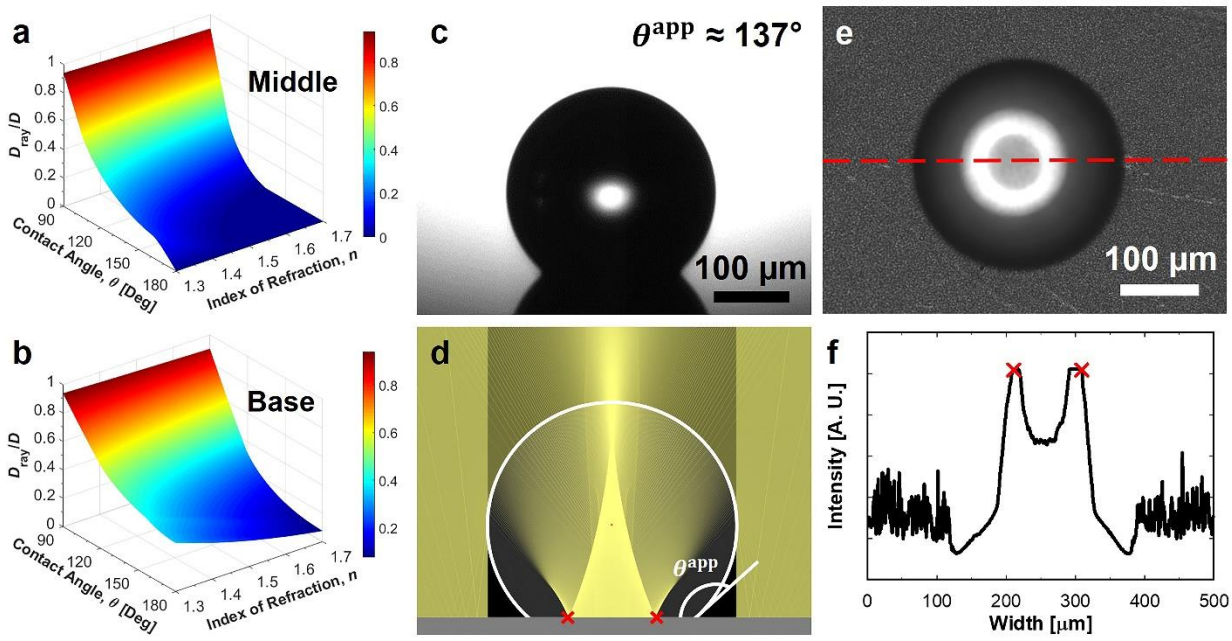

Figure 7. Regime map of ray optics simulation as a function of refractive index for a common working fluid ($1.3 < n < 1.7$) when focal plane is placed at (a) the middle and (b) the bottom of the droplet. (c) Side-view image taken with classical microgoniometry of a microscopic ethylene glycol droplet (EG, $C_2H_6O_2$, $\gamma \approx 47$ mN/m, $n \approx 1.43$) residing on an HTMS-coated nanostructured boehmite surface showing apparent contact angle of ≈137°. (d) Ray optics simulation through the EG droplet with $\theta^{app} = 137°$ and $n = 1.43$. (e) Top-view optical microscopy image of the EG droplet with (f) corresponding intensity profiles along the red-dotted line segment shown in (e). Note, the EG droplets in (c) and (e) are the same.

The present work demonstrates comprehensive *in situ* contact angle measurement techniques using optical microscopy. Each technique has its own advantages. The developed FPSI and ray optics methods work well for hydrophobic surfaces, while the wave interference method

is advantageous for hydrophilic surfaces. With respect to the data acquisition speed, the ray optics method is instantaneous (limited by the speed of the imaging method) and can be integrated with high-speed imaging approaching data acquisition rates of 1 MHz. However, the FPSI method is relatively slow, while the wave optics method can afford intermediate frame rate imaging. The FPSI technique can measure the contact angle of liquid droplet having unknown material properties such as index of refraction, since it only utilizes the droplet geometry. The ray optics method is capable of measuring contact angles for fluids of various indices of refraction (Fig. 7a, b). Figure 7c shows a microscopic ethylene glycol ($C_2H_6O_2$, $\gamma \approx 47$ mN/m) droplet residing on an HTMS-coated nanostructured boehmite surface. We specifically chose ethylene glycol (EG) due to its different index of refraction, $n \approx 1.43$, and low vapor pressure (< 100 Pa). Ray optics simulations revealed $D_{\mathrm{ray}}/D \approx 0.35$ for droplets with $\theta^{\mathrm{app}} = 137°$ (Fig. 7d). A particular EG droplet showed $D \approx 272$ µm and $D_{\mathrm{ray}} \approx 98$ µm (Fig. 7e, f), resulting in $D_{\mathrm{ray}}/D \approx 0.36$ and corresponding $\theta^{\mathrm{app}} \approx 136°$. The results show that in addition to characterizing apparent contact angle, the refractive index of an unknown fluid can be estimated using the ray optics method.

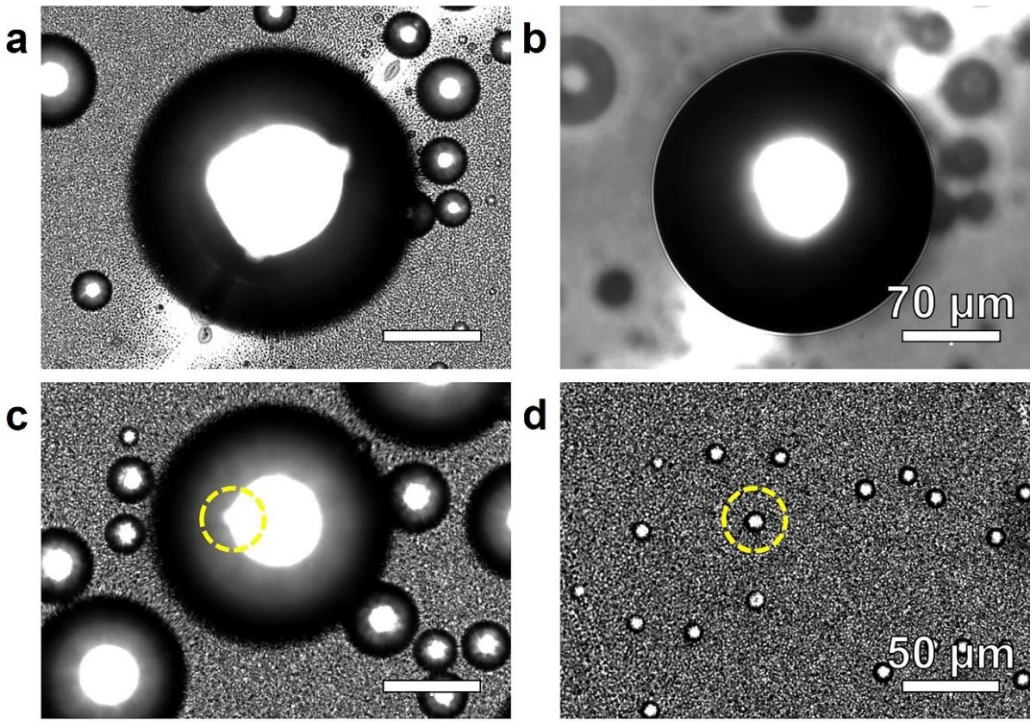

Figure 8. Top-view optical microscopy images of droplets residing on the nanostructured superhydrophobic boehmite surface with the focal plane placed at (a) the bottom and (b) the middle of the droplet. The contact angle measurement using the FPSI technique showed a decreased apparent advancing contact angle of θ_a^{app}≈145° due to the presence of the defect. (c) Top-view optical microscopy image of a droplet residing on the superhydrophobic surface on a nanoscale defect during condensation. Although the nanoscale defect was not visible with top-view optical microscopy, it acted as a preferential nucleation site during consecutive condensation cycles as shown in (d).

Moreover, the ray optics method can be used to detect micro/nanoscale surface degradation and defects. We showed that the shape of the ray at the bottom of the droplet is clearly circular despite diffuse reflection from the rough surface. However, if the droplet condenses on a microscale defect site on a surface, the shape of the concentrated ray is clearly deformed. Figure 8a, b and S1b show the droplet condensing on a microscale scratch on a superhydrophobic surface. The results show that the concentrated ray is clearly deformed on the surface, rendering the ray optics method incapable of measuring the apparent contact angle. The FPSI method showed a reduced apparent contact angle of ≈145° due to the presence of the defect. Note that the contact

angle was determined by Eq. (1) using the radius of curvature, R, and middle-to-base distance, L, therefore the local contact angle around the nonuniformly deformed contact line may vary. Furthermore, nanoscale defect sites may not be observable with optical microscopy. However, the liquid contact line can pin on the unobservable defects, resulting concentrated ray deformation at the bottom of the droplet (Fig. 8c). Although the nanoscale defect did not affect the characterization of the apparent contact angle, it acted as a preferential nucleation site during subsequent condensation cycles (Fig. 8d).

In the future, it would be interesting to enable the use of the interferometry method for a wider range of apparent contact angle. From a theoretical standpoint, it is possible to measure higher apparent contact angles ($\theta^{\mathrm{app}} > 90°$) using droplet geometry and interferometric fringes by $\theta^{\mathrm{app}} = \pi/2 + \sin^{-1}(\Delta h/\Delta R - 1)$. However, measuring the apparent contact angle becomes more difficult for spherical droplets due to the presence of larger droplet height variation at the droplet center coupled with the distance between fringes reaching the maximum resolution of the microscope. For droplets having $\theta^{\mathrm{app}} > 90°$, longer wavelength light can be used. For example, when red light ($\lambda \approx 700$ nm) is used, the height difference between two fringes is $h \approx 263$ nm, much larger than that of blue light $h \approx 163$ nm. Hence, utilization of longer wavelengths results in larger height variations and easier recognition of the corresponding distance between fringes.

CONCLUSIONS

In summary, we developed single-camera optical imaging techniques for the measurement of droplet apparent contact angle. We demonstrated the FPSI method by manipulating the focal plane on hydrophobic and superhydrophobic surfaces. In addition, we utilized ray optics simulations to predict the path of the rays through the droplet and related the apparent contact angle to the ratio

between droplet and ray diameters. For hydrophilic surfaces, we developed a modified wave interference technique by obtaining relative growth of interferometric fringes at the center of the droplet. Our techniques are integratable with existing optical microscopy platforms, with minimal change required, and were benchmarked with *in situ* contact angle measurements and comparison with classical microgoniometry. The outcomes of this work establish a simple but powerful tool to more easily characterize microscale apparent advancing and receding contact angles of arbitrary liquid droplets.

METHODS

Surface Fabrication. Smooth silicon (Si) wafers (P/B <100> orientation 0-100 Ω-cm, University Wafer) and boehmite (AlO(OH)) surfaces were used as model substrates for hydrophobic and superhydrophobic surfaces, respectively. To create nanostructured boehmite surfaces, 250 nm-thick aluminum (Al, 99.999%) layer was deposited on a polished Si wafer in a magnetron sputtering system (AJA Orion-8 Magnetron) under chamber pressure of 3 mTorr, RF power of 200W, and Argon mass flow rate of 30 sccm. Al-coated Si wafer and aluminum tabs (99.0 % purity, 20 mm x 20 mm x 0.8 mm, McMaster-Carr) were immersed into hot water (≈90 °C) for 1 hour. At the surface of the samples, nanostructured boehmite surfaces with sharp and knife-like structures were formed having length scales approaching ≈90 nm. To functionalize the surfaces, heptadecafluorodecyltrimethoxy-silane (HTMS, CAS no. 83048-65-1, Dow Corning Co.) was deposited on both the smooth Si wafer and the nanostructured boehmite surfaces using vapor phase deposition. Samples were first rinsed with acetone, isopropyl alcohol (IPA), deionized (DI) water, dried in a clean nitrogen (N_2) flow, and cleaned with plasma cleaner. Then, samples and a 50 mL beaker containing 1 mL of HTMS toluene solution (5% v/v) were sealed in a glass container and

heated in an atmospheric pressure oven (Lindberg Blue M) at 80°C for 3 hours. This process allowed for the development of a highly conformal (monolayer thick) silane layer on surfaces. Microgoniometric measurements (MCA-3, Kyowa Interface Science) of ≈100 nL droplets on the hydrophobic Si surface and superhydrophobic boehmite surfaces showed apparent advancing and receding contact angle of θ_a = 114.9 ± 1.3°/θ_r = 107.4 ± 1.4° and θ_a = 164.9 ± 0.7°/θ_r = 162.9 ± 0.6°, respectively.

To prepare the hydrophilic surfaces, thermally grown silica substrates (*p*-type, 3 inch, <100> orientation, 0-100 Ω-cm, University wafer) with 1150 nm oxide layers were degreased by rinsing in acetone, IPA, DI water, and dried with a clean N_2 flow. Polymethyl methacrylate (PMMA, CAS no. 100-66-3, MicroChem) was spun-coated on the Si wafer for 45 seconds at 2,000 RPM, followed by pre-baking on a hot plate (3581201 C-MAG HS 7 IKAMAG Glass Ceramics, IKA) at 180°C for 50 seconds. Ellipsometry measurements of the PMMA thin film showed a thickness of 170 ± 5 nm (Woollam VAS Ellipsometer). Microgoniometric measurements of ≈50 nL droplets on PMMA coated Si showed apparent advancing and receding contact angles of θ_a = 69 ± 1° and θ_r = 40 ± 1°, respectively.

Surface Characterization. Atomic force microscopy (Cypher, Asylum Research) was performed in tapping mode on all samples using a cantilever with a tip radius <10 nm (Tap300AL-G, TED PELLA, INC.). Field emission scanning electron microscopy (Scios 2 DualBeam, FEI) was performed on nanostructured boehmite surfaces at an imaging voltage range of 10.0 to 20.0 kV and a beam current range of 10.0 to 20.0 μA. Contact angle measurements of ≈50 nL droplets on all samples were performed using a microgoniometer (MCA-3, Kyowa Interface Science).

Condensation Experiment. Water vapor condensation experiments were performed using conventional microscopy. A monochrome camera (DS-Qi2, Nikon) was attached to an optical

microscope (Eclipse LV100, Nikon) for top-view analysis. Illumination was supplied by a light emitting diode (LED) light source (SOLA SM II Light Engine, Lumencor). The LED light source was specifically chosen for its high-intensity, low-power consumption (2.5 W) and narrow spectral range (380−680 nm) in order to minimize heat generation at the surface. Samples were horizontally placed on a cold stage (TP104SC-mK2000A, Instec) by applying a thin layer of thermal grease (Omegatherm, Omega, thermal conductivity of 2.2 W/(m·K)), followed by reducing temperature to T_w = 1 ± 0.5°C to induce condensation and increasing temperature to T_w = 30 ± 0.5°C to induce the evaporation in a laboratory air environment having temperature T_{air} = 23 ± 0.5°C and a relative humidity ϕ = 45 ± 5% (RO120, Roscid). To demonstrate the optical interference, a collimated beam of white light laser was filtered using a bandpass excitation filter (λ = 435 ± 10 nm, ECFP/Cerulean Filter Set, Nikon). Imaging was performed with a 20X (TU Plan Fluor EPI, Nikon), 50X (TU Plan EPI ELWD, Nikon), and 100X (TU Plan EPI ELWD, Nikon) objectives.

Ray Optics Simulation. Two-dimensional (2D) axisymmetric ray optics simulation was performed using both an open source simulation platform[41] and MATLAB (R2018a, Mathworks). The circular segment of a droplet having an apparent contact angle with a defined refractive index was placed on top of a reflective flat substrate. A collimated beam of light rays emanating from the horizontal wall bounding the top of the simulation was applied. Contact angle and index of refraction were varied throughout the simulation.

ASSOCIATED CONTENT

The authors declare no competing financial interest.

Supporting Information

The supporting information is available free of charge on the ACS Publication website at DOI:

Further information about scanning electron microscopy, intensity profile as a function of focal plane location, schematic of diffuse reflection on a nanostructured surface, ray trajectory through a hydrophilic droplet, schematic of hydrophilic droplet, and cost breakdown of state-of-the-art goniometric systems. (PDF)

Video S1: Two-dimensional axisymmetric ray optics simulation of light rays propagating through the liquid droplet on a surface for the entire range of apparent contact angle from 0° to 180° (MP4)

Video S2: Experimental top-view optical microscopy showing condensation and evaporation of a water droplet on a PMMA coated Si wafer (MP4)

AUTHOR INFORMATION

Corresponding Author

*E-mail: nmiljkov@illinois.edu

ORCID

Hyeongyun Cha: 000-0001-7157-7315

Jingcheng Ma: 0000-0002-0473-5042

Young Seong Kim: 0000-0002-2132-1108

Longnan Li: 0000-0003-0225-3303

Luwen Sun: 0000-0002-4959-9638

Jiashuo Tong: 0000-0002-3175-8450

Nenad Miljkovic: 0000-0002-0866-3680

Author Contributions

H.C. and N.M. conceived the initial idea for this research. N.M. guided the work. H.C., J.M., L.L., L.S., and J.T. conducted parts of the fabrication and experiments. H.C. and Y.S.K conducted the numerical simulation. All authors were responsible for writing the paper and have given approval to the final version of the manuscript.

ACKNOWLEDGEMENTS

The authors acknowledge Jungeun Won of UIUC for discussion on optics. The authors gratefully acknowledge funding support from the Office of Naval Research (ONR) (Grant No. N00014-16-1-2625). The authors also gratefully acknowledge funding support from the International Institute for Carbon Neutral Energy Research (WPI-I2CNER), sponsored by the Japanese Ministry of Education, Culture, Sports, Science and Technology. Atomic force microscopy was carried out in part in the Materials Research Laboratory Central Facilities, University of Illinois.

REFERENCES

(1) Blossey, R. Self-Cleaning Surfaces — Virtual Realities. *Nat. Mater.* **2003**, 2, 301-306.
(2) Wang, J. Z.; Zheng, Z. H.; Li, H. W.; Huck, W. T. S.; Sirringhaus, H. Dewetting of Conducting Polymer Inkjet Droplets on Patterned Surfaces. *Nat. Mater.* **2004**, 3, 171-176.
(3) Dunn, A. C.; Pitenis, A. A.; Urueña, J. M.; Schulze, K. D.; Angelini, T. E.; Sawyer, W. G. Kinetics of Aqueous Lubrication in the Hydrophilic Hydrogel Gemini Interface. *Proc. Inst. Mech. Eng., Part H* **2015**, 229, 889-894.
(4) Gau, H.; Herminghaus, S.; Lenz, P.; Lipowsky, R. Liquid Morphologies on Structured Surfaces: From Microchannels to Microchips. *Science* **1999**, 283, 46-49.
(5) Bauer, J.; Drescher, G.; Illig, M. Surface Tension, Adhesion and Wetting of Materials for Photolithographic Process. *J. Vac. Sci. Technol., B: Microelectron. Nanometer Struct.--Process., Meas., Phenom.* **1996**, 14, 2485-2492.
(6) Rose, J. W. Dropwise Condensation Theory and Experiment: A Review. *Proc. Inst. Mech. Eng., Part A* **2002**, 216, 115-128.

(7) Young, T. An Essay on the Cohesion of Fluids. *Philos. Trans. R. Soc. London* **1805**, 95, 65-87.
(8) Drelich, J. W.; Boinovich, L.; Chibowski, E.; Della Volpe, C.; Hołysz, L.; Marmur, A.; Siboni, S. Contact Angles: History of over 200 Years of Open Questions. *Surf. Innovations* **2019**, 0, 1-25.
(9) Wenzel, R. N. Resistance of Solid Surfaces to Wetting by Water. *Ind. Eng. Chem.* **1936**, 28, 988-994.
(10) Cassie, A. B. D.; Baxter, S. Wettability of Porous Surfaces. *Trans. Faraday Soc.* **1944**, 40, 546-551.
(11) Drelich, J. W. Contact Angles: From Past Mistakes to New Developments through Liquid-Solid Adhesion Measurements. *Adv. Colloid Interface Sci.* **2019**, 267, 1-14.
(12) de Gennes, P. G. Wetting: Statics and Dynamics. *Rev. Mod. Phys.* **1985**, 57, 827-863.
(13) Gao, L.; McCarthy, T. J. Contact Angle Hysteresis Explained. *Langmuir* **2006**, 22, 6234-6237.
(14) Wisdom, K. M.; Watson, J. A.; Qua, X.; Liua, F.; Watson, G. S.; Chen, C. H. Self-Cleaning of Superhydrophobic Surfaces by Self-Propelled Jumping Condensate. *Proc. Natl. Acad. Sci. U. S. A.* **2013**, 110, 7992–7997.
(15) Boreyko, J. B.; Collier, P. C. Delayed Frost Growth on Jumping-Drop Superhydrophobic Surfaces. *ACS Nano* **2013**, 7, 1618-1627.
(16) Miljkovic, N.; Enright, R.; Nam, Y.; Lopez, K.; Dou, N.; Sack, J.; Wang, E. N. Jumping-Droplet-Enhanced Condensation on Scalable Superhydrophobic Nanostructured Surfaces. *Nano Lett.* **2013**, 13, 179-187.
(17) Wilhelmy, L. Ueber die Abhängigkeit der Capillaritäts-Constanten des Alkohols von Substanz und Gestalt des benetzten festen Körpers. *Annalen der Physik* **1863**, 195, 177-217.
(18) Della Volpe, C.; Siboni, S. The Wilhelmy Method: A Critical and Practical Review. *Surf. Innovations* **2018**, 6, 120-132.
(19) Drelich, J. Guidelines to Measurements of Reproducible Contact Angles Using a Sessile-Drop Technique. *Surf. Innovations* **2013**, 1, 248-254.
(20) Extrand, C. W. Contact Angles and Hysteresis on Surfaces with Chemically Heterogeneous Islands. *Langmuir* **2003**, 19, 3793-3796.
(21) Huhtamäki, T.; Tian, X.; Korhonen, J. T.; Ras, R. H. A. Surface-Wetting Characterization Using Contact-Angle Measurements. *Nat. Protoc.* **2018**, 13, 1521-1538.
(22) Chen, H.; Muros-Cobos, J. L.; Amirfazli, A. Contact Angle Measurement with a Smartphone. *Rev. Sci. Instrum.* **2018**, 89, 035117.
(23) Günay, A. A.; Sett, S.; Oh, J.; Miljkovic, N. Steady Method for the Analysis of Evaporation Dynamics. *Langmuir* **2017**, 33, 12007-12015.
(24) Yan, X.; Huang, Z.; Sett, S.; Oh, J.; Cha, H.; Li, L.; Feng, L.; Wu, Y.; Zhao, C.; Orejon, D.; Chen, F.; Miljkovic, N. Atmosphere-Mediated Superhydrophobicity of Rationally Designed Micro/Nanostructured Surfaces. *ACS Nano* **2019**, 13, 4160-4173.
(25) Papadopoulos, P.; Mammen, L.; Deng, X.; Vollmer, D.; Butt, H.-J. How Superhydrophobicity Breaks Down. *Proc. Natl. Acad. Sci.* **2013**, 110, 3254-3258.
(26) Schellenberger, F.; Encinas, N.; Vollmer, D.; Butt, H.-J. How Water Advances on Superhydrophobic Surfaces. *Phys. Rev. Lett.* **2016**, 116, 096101.
(27) Pawley, J. *Handbook of Biological Confocal Microscopy*. 3 ed.; Springer: Boston, MA, **2010**.

(28) Awasthi, A.; Bhatt, Y. J.; Garg, S. P. Measurement of Contact Angle in Systems Involving Liquid Metals. *Meas. Sci. Technol.* **1996**, 7, 753-757.

(29) Zhang, N.; Chao, D. F. A New Laser Shadowgraphy Method for Measurements of Dynamic Contact Angle and Simultaneous Flow Visualization in a Sessile Drop. *Opt. Laser Technol.* **2002**, 34, 243-248.

(30) Tachon, L.; Guignard, S. An Accurate Optical Method for the Measurement of Contact Angle and Interface Shape of Evaporative Thin Liquids Films. *Exp. Therm. Fluid Sci.* **2018**, 90, 66-75.

(31) Allain, C.; Ausserre, D.; Rondelez, F. A New Method for Contact-Angle Measurements of Sessile Drops. *J. Colloid Interface Sci.* **1985**, 107, 5-13.

(32) Sundberg, M.; Månsson, A.; Tågerud, S. Contact Angle Measurements by Confocal Microscopy for Non-Destructive Microscale Surface Characterization. *J. Colloid Interface Sci.* **2007**, 313, 454-460.

(33) Campbell, J. M.; Christenson, H. K. Dynamic Measurement of Low Contact Angles by Optical Microscopy. *ACS Appl. Mater. Interfaces* **2018**, 10, 16893-16900.

(34) Cha, H.; Chun, J. M.; Sotelo, J.; Miljkovic, N. Focal Plane Shift Imaging for the Analysis of Dynamic Wetting Processes. *ACS Nano* **2016**, 10, 8223-8232.

(35) Cha, H.; Chun, J. M.; Xu, Y.; Miljkovic, N. Focal Plane Shift Imaging for the Analysis of Multi-Droplet Jumping. *J. Heat Transfer* **2017**, 139, 020903.

(36) Vedder, W.; Vermilyea, D. A. Aluminum + Water Reaction. *Trans. Faraday Soc.* **1969**, 65, 561-584.

(37) Tadanaga, K.; Katata, N.; Minami, T. Super-Water-Repellent Al2O3 Coating Films with High Transparency. *J. Am. Ceram. Soc.* **1997**, 80, 1040-1042.

(38) Yang, Z.; Wu, Y.-Z.; Ye, Y.-F.; Gong, M.-G.; Xu, X.-L. A Simple Way to Fabricate an Aluminum Sheet with Superhydrophobic and Self-Cleaning Properties. *Chin. Phys. B* **2012**, 21, 126801.

(39) Chavan, S.; Cha, H.; Orejon, D.; Nawaz, K.; Singla, N.; Yeung, Y. F.; Park, D.; Kang, D. H.; Chang, Y.; Takata, Y.; Miljkovic, N. Heat Transfer through a Condensate Droplet on Hydrophobic and Nanostructured Superhydrophobic Surfaces. *Langmuir* **2016**, 32, 7774-7787.

(40) Cha, H.; Wu, A.; Kim, M.-K.; Saigusa, K.; Liu, A.; Miljkovic, N. Nanoscale-Agglomerate-Mediated Heterogeneous Nucleation. *Nano Lett.* **2017**, 17, 7544-7551.

(41) Tu, R. Ray Optics Simulation. at https://ricktu288.github.io/ray-optics/ (accessed 1 April, 2019).

(42) Haynes, W. M. *CRC Handbook of Chemistry and Physics*. 95 ed.; CRC press: Boca Raton, FL, **2014**.

(43) Stöckelhuber, K. W.; Radoev, B.; Schulze, H. J. Some New Observations on Line Tension of Microscopic Droplets. *Colloids Surf., A* **1999**, 156, 323-333.

(44) van der Veen, R. C. A.; Tran, T.; Lohse, D.; Sun, C. Direct Measurements of Air Layer Profiles under Impacting Droplets Using High-Speed Color Interferometry. *Phys. Rev. E* **2012**, 85, 026315.

(45) Bouillant, A.; Mouterde, T.; Bourrianne, P.; Lagarde, A.; Clanet, C.; Quéré, D. Leidenfrost Wheels. *Nat. Phys.* **2018**, 14, 1188-1192.

(46) Sett, S.; Sinha-Ray, S.; Yarin, A. L. Gravitational Drainage of Foam Films. *Langmuir* **2013**, 29, 4934-4947.

(47) Gokhale, S. J.; Plawsky, J. L.; Wayner, P. C. Experimental Investigation of Contact Angle, Curvature, and Contact Line Motion in Dropwise Condensation and Evaporation. *J. Colloid Interface Sci.* **2003**, 259, 354-366.
(48) Yahiaoui, R.; Danaie, K.; Petitgrand, S.; Bosseboeuf, A. Automated Interferometric System for Bulge and Blister Test Measurements of Micromachined Membranes, in *Proceedings of the SPIE*, **2001**, 4400, 160-169.
(49) Cao, Z.; Wang, P.; Gao, W.; Tao, L.; Suk, J. W.; Ruoff, R. S.; Akinwande, D.; Huang, R.; Liechti, K. M. A Blister Test for Interfacial Adhesion of Large-Scale Transferred Graphene. *Carbon* **2014**, 69, 390-400.
(50) Ma, J.; Cha, H.; Kim, M.-K.; Cahill, D. G.; Miljkovic, N. Condensation Induced Delamination of Nanoscale Hydrophobic Films. *Adv. Funct. Mater.* **2019**, 0, 1905222.
(51) McHale, G.; Rowan, S. M.; Newton, M. I.; Banerjee, M. K. Evaporation and the Wetting of a Low-Energy Solid Surface. *J. Phys. Chem. B* **1998**, 102, 1964-1967.
(52) Deegan, R. D.; Bakajin, O.; Dupont, T. F.; Huber, G.; Nagel, S. R.; Witten, T. A. Contact Line Deposits in an Evaporating Drop. *Phys. Rev. E* **2000**, 62, 756-765.
(53) Park, J. K.; Ryu, J.; Koo, B. C.; Lee, S.; Kang, K. H. How the Change of Contact Angle Occurs for an Evaporating Droplet: Effect of Impurity and Attached Water Films. *Soft Matter* **2012**, 8, 11889-11896.
(54) Egner, A.; Hell, S. W. Fluorescence Microscopy with Super-Resolved Optical Sections. *Trends Cell Biol.* **2005**, 15, 207-215.
(55) Taylor, J. R. *Introduction to Error Analysis, The Study of Uncertainties in Physical Measurements*. 2nd ed.; University Science Books: Sausalito, California, **1997**.
(56) Law, B. M.; McBride, S. P.; Wang, J. Y.; Wi, H. S.; Paneru, G.; Betelu, S.; Ushijima, B.; Takata, Y.; Flanders, B.; Bresme, F.; Matsubara, H.; Takiue, T.; Aratono, M. Line Tension and Its Influence on Droplets and Particles at Surfaces. *Prog. Surf. Sci.* **2017**, 92, 1-39.
(57) Drelich, J. The Significance and Magnitude of the Line Tension in Three-Phase (Solid-Liquid-Fluid) Systems. *Colloids Surf., A* **1996**, 116, 43-54.

For Table of Contents Only